




# Edge-Averaged Virtual Element Methods for Convection-Diffusion and Convection-Dominated Problems

Shuhao Cao<sup>1</sup> · Long Chen<sup>2</sup> · Seulip Lee<sup>3</sup> 

Received: 30 December 2024 / Revised: 21 June 2025 / Accepted: 25 June 2025

© The Author(s), under exclusive licence to Springer Science+Business Media, LLC, part of Springer Nature 2025

## Abstract

This paper develops edge-averaged virtual element (EAVE) methodologies to address convection-diffusion problems effectively in the convection-dominated regime. It introduces a variant of EAVE that ensures monotonicity (producing an  $M$ -matrix) on Voronoi polygonal meshes, provided their duals are Delaunay triangulations with acute angles. Furthermore, the study outlines a comprehensive framework for EAVE methodologies, introducing another variant that integrates with the stiffness matrix derived from the lowest-order virtual element method for the Poisson equation. Numerical experiments confirm the theoretical advantages of the monotonicity property and demonstrate an optimal convergence rate across various mesh configurations.

**Keywords** Virtual elements · Edge-averaged finite element · Steady-state convection-diffusion equation · Monotone schemes · Convection-dominated problems · Polygonal meshes

**Mathematics Subject Classification** 65N30 · 65N12

---

✉ Seulip Lee  
seulip.lee@tufts.edu

Shuhao Cao  
scao@umkc.edu

Long Chen  
lchen7@uci.edu

<sup>1</sup> School of Science and Engineering, University of Missouri-Kansas City, Kansas City, MO 64110, USA

<sup>2</sup> Department of Mathematics, University of California at Irvine, Irvine, CA 92697, USA

<sup>3</sup> Department of Mathematics, Tufts University, Medford, MA 02155, USA

## 1 Introduction

We consider the convection-diffusion equation in a bounded domain  $\Omega \subset \mathbb{R}^2$  with the simply-connected polygonal Lipschitz boundary  $\partial\Omega$ :

$$-\nabla \cdot (\alpha(\mathbf{x})\nabla u + \beta(\mathbf{x})u) = f \quad \text{in } \Omega, \quad (1.1a)$$

$$u = 0 \quad \text{on } \partial\Omega, \quad (1.1b)$$

where  $\alpha \in C^0(\bar{\Omega})$  with  $0 < \alpha_{\min} \leq \alpha(\mathbf{x}) \leq \alpha_{\max}$  for every  $\mathbf{x} \in \Omega$ ,  $\beta \in (C^0(\bar{\Omega}))^2$ , and  $f \in L^2(\Omega)$ . The convection-diffusion problem (1.1) expresses the convective and molecular transport along a stream moving at the given velocity  $\beta$  and with the diffusive effect from  $\alpha$ . The convection-dominated regime means the situation that

$$\alpha(\mathbf{x}) \ll |\beta(\mathbf{x})|, \quad \forall \mathbf{x} \in \Omega,$$

and the convection-diffusion problem in this regime is important in describing viscous fluid models with high Reynolds numbers governed by the Navier-Stokes equations (e.g., [20, 28]).

It has long been known that the standard-conforming finite element method (FEM) fails to provide accurate numerical solutions for convection-dominated problems. The finite element solutions based on standard Galerkin projections contain spurious oscillations that deteriorate the solutions' quality (e.g., see [22, 27, 29, 41]). Hence, various stabilized FEMs have been developed in two primary directions. The first direction is based on presenting a provable order of convergence in appropriate norms independent of small  $\alpha$  by adding stabilization terms to the weak formulation. This category includes the streamline-upwind Petrov-Galerkin (SUPG) methods [10], continuous interior penalty methods [12], and local projection stabilization (LPS) methods [31]. This stabilization technique mitigates such unexpected oscillations but does not eliminate them. The second direction is the development of stabilized methods satisfying the discrete maximum principle (DMP). When solving a second-order elliptic equation numerically, it is known that a numerical scheme satisfying the DMP guarantees discrete solutions without spurious oscillations (see, e.g., [11, 19, 39]). Among many examples, the algebraic flux corrections (AFC) method [4] is an upwind-based discretization that directly satisfies the DMP with a reduced artificial diffusion effect, but it requires solving a nonlinear system. The monotonicity property [24] is a sufficient condition for the DMP, so monotone schemes have received attention despite their first-order convergence when  $\alpha = 0$  [25]. Moreover, getting a non-singular  $M$ -matrix in a discretization implies the monotonicity property. Such an  $M$ -matrix is characterized by nonpositive off-diagonal entries and diagonal dominance, including at least one strictly diagonally dominant column. We note that this  $M$ -matrix condition makes it easier to validate the DMP.

The edge-averaged finite element (EAFE) method [32, 53] is a well-known linear monotone FEM, and it has been recently applied to space-time discretization [3] and nearly inviscid incompressible flows [35]. The EAFE method is monotone if the stiffness matrix of the linear conforming FEM for the Poisson equation is an  $M$ -matrix, achieved by a Delaunay triangulation in two dimensions. The EAFE method has been motivated by prior studies of the Scharfetter-Gummel method [40], including its finite volume formulation [2], the exponential fitting approach [8, 9, 21], and the inverse-average-type finite element method [37]. A high-order Scharfetter-Gummel discretization was derived in the finite element setting (see [3]), where monotonicity is only preserved in the lowest-order case (corresponding to the EAFE method). This idea has recently been extended to a general framework for scalar and vector convection-diffusion problems, called the simplex-averaged finite element (SAFE) meth-

ods [52]. A stable mimetic finite difference (MFD) method [1] has also been presented in the SAFE framework. However, none of these methods work for general polygonal meshes because translating the conformity of the polynomial elements on simplices to polygons is not straightforward. For this reason, our work proposes a generalization of the EAFE method compatible with virtual element methods on polygonal meshes.

Virtual element methods (VEMs), a generalization of FEMs, are novel numerical PDE methods on general polygonal and polyhedral meshes. The VEMs use a non-polynomial approximation in a polygonal element, and exact pointwise values of local basis functions are not needed inside the element. Instead, the degrees of freedom (DoFs) can be used to compute all necessary quantities to build a stable and accurate discretization. More details can be found in references [43, 46] and Section 3 in this paper.

This paper focuses on developing stabilized VEMs for convection-dominated problems, with particular attention to the lowest-order case to investigate the preservation of the monotonicity property of VEMs. Stabilization techniques such as the streamline upwind Petrov-Galerkin (SUPG) method and local projection stabilization (LPS) have been successfully incorporated into VEMs in [5, 6, 50] and [34], respectively. However, these approaches do not guarantee the DMP, potentially resulting in non-physical oscillations in the numerical solution. To address this limitation, we propose a generalization of the EAFE stabilization to the VEM framework, leading to a class of methods we refer to as edge-averaged virtual element (EAVE) methods. We present two variants of the EAVE method: **(1)** a monotone EAVE method designed for Voronoi meshes with dual Delaunay and **(2)** A general EAVE method applicable to arbitrary polygonal meshes.

**(1)** The monotone EAVE method guarantees the DMP on Voronoi meshes with dual Delaunay triangulations consisting of acute triangles. Furthermore, its bilinear form does not require a stabilization term commonly inherent in virtual element methods. The basic idea of deriving this method is utilizing flux approximations and dual edge patches for mass lumping inspired by references [53] and [7], respectively.

**(2)** The general EAVE method extends the EAFE-based stabilization to virtual elements on general polygonal meshes. Its monotonicity property holds if the stiffness matrix of the linear VEM for the Poisson equation is an  $M$ -matrix. To construct the bilinear form, we define a flux approximation in the lowest-order  $H(\mathbf{curl})$ -conforming virtual element space and observe the relationship between the lowest-order  $H(\mathbf{curl})$ - and linear  $H^1$ -conforming spaces.

Through numerical experiments, we observe that both EAVE schemes produce stable and accurate solutions and achieve first-order convergence on various polygonal mesh types, while the monotone EAVE method gives slightly better results when applied to the same Voronoi meshes. Finally, we compare the numerical performance of the proposed EAVE methods with other stabilized techniques, confirming their robustness and first-order accuracy.

The remaining sections are structured: Section 2 introduces necessary notations and observes the EAFE stabilization's main idea. The essential definitions and theoretical aspects of the VEMs are introduced in Section 3. In Section 4, we present a finite-volume bilinear form for the Poisson equation compatible with a virtual element space and stabilization-free, providing fundamental ideas of using dual edge patches for mass lumping. Section 5 proposes a monotone EAVE method on Voronoi meshes with dual Delaunay triangulations consisting of acute triangles. Section 6 introduces a general EAVE method for arbitrary polygonal meshes and provides a sufficient condition for ensuring monotonicity. In Section 7, our numerical experiments show the effect of edge-averaged stabilization on VEMs as well as the optimal order of convergence on different mesh types. Finally, we summarize our contribution in this paper and discuss related research in Section 8.

## 2 Preliminaries

To begin with, we introduce some notation used throughout this paper. For a bounded Lipschitz domain  $\mathcal{D} \in \mathbb{R}^2$ , we denote the Sobolev space of  $L^2$ -integrable up to  $m$ -th weak derivatives as  $H^m(\mathcal{D})$ , and the space  $H^0(\mathcal{D})$  coincides with  $L^2(\mathcal{D})$ , where the norm and seminorm are denoted by  $\|\cdot\|_{H^m(\mathcal{D})}$  and  $|\cdot|_{H^m(\mathcal{D})}$ , respectively. The notation  $H_0^1(\mathcal{D})$  means the space of  $v \in H^1(\mathcal{D})$  such that  $v = 0$  on  $\partial\mathcal{D}$  in the trace sense. The polynomial spaces of degrees less than or equal to  $k$  are denoted as  $\mathcal{P}_k(\mathcal{D})$ , and the space of continuous functions is denoted as  $C^0(\mathcal{D})$ .

### 2.1 Model Problem

In the convection-diffusion equation (1.1a), we denote the flux as

$$J(u) := \alpha \nabla u + \beta u.$$

The weak formulation of the problem (1.1) is to find  $u \in H_0^1(\Omega)$  such that

$$B(u, v) = F(v), \quad \forall v \in H_0^1(\Omega), \quad (2.1)$$

where the bilinear form and the functional on the right-hand side are defined as

$$B(w, v) := \int_{\Omega} J(w) \cdot \nabla v \, dx \quad \text{and} \quad F(v) := \int_{\Omega} f v \, dx.$$

The well-posedness of the continuous problem (2.1) can be found in [24].

### 2.2 Exponential Fitting of the Flux

If there exists a potential function  $\psi$  such that  $\nabla\psi = \alpha^{-1}\beta$ , then the flux  $J(u)$  can be expressed as a diffusion flux with a variable coefficient,

$$J(u) = \kappa \nabla(e^{\psi}u) \quad \text{with} \quad \nabla\psi = \alpha^{-1}\beta, \quad \kappa(\mathbf{x}) = \alpha(\mathbf{x})e^{-\psi(\mathbf{x})}.$$

In terms of differential forms,  $e^{\psi}u$  is a 0-form,  $\nabla(e^{\psi}u)$  is a 1-form,  $J(u)$  is a 2-form, and  $\kappa$  is a Hodge star mapping a 1-form to a 2-form.

If  $\alpha$  and  $\beta$  are constant, the function  $\psi$  is defined as  $\psi(\mathbf{x}) = \alpha^{-1}\beta \cdot \mathbf{x}$ , and it is unique up to a constant. However, such a potential function  $\psi$  may not exist for general  $\alpha$  and  $\beta$  if  $\text{curl}(\alpha^{-1}\beta) \neq 0$ .

A proper flux approximation [32, 53] is defined in the lowest order Nédélec space on triangular meshes, and it has been successfully applied to develop the edge-averaged finite element (EAFE) scheme. In what follows, we briefly explain the main idea of the EAFE scheme on a triangulation.

### 2.3 Flux Approximations

Let  $\mathcal{T}_h$  be a conforming triangulation for  $\Omega$  and  $V_h = \mathcal{P}_1(\mathcal{T}_h)$  be the piecewise linear  $H^1$ -conforming finite element space. We consider the local flux  $J(u_h)|_T = (\alpha \nabla u_h + \beta u_h)|_T$  for  $u_h \in V_h$  and  $T \in \mathcal{T}_h$ .

We define  $\tau_E$  as a scaled tangent vector of  $E$  with  $|\tau_E| = |E|$ . Suppose  $\mathbf{x}(t)$  is a parametrization of  $E$  such that  $\mathbf{x}(0) = \mathbf{x}_i$  and  $\mathbf{x}(1) = \mathbf{x}_j$  are two endpoints of  $E$ . Let us

define

$$\psi_E(\mathbf{x}(t)) = \int_0^t \frac{1}{|E|} \alpha^{-1}(\boldsymbol{\beta} \cdot \boldsymbol{\tau}_E) \, ds, \quad \kappa_E = \alpha e^{-\psi_E} > 0. \quad (2.2)$$

Then, it follows

$$J(u_h) \cdot \boldsymbol{\tau}_E|_E = \kappa_E \nabla(e^{\psi_E} u_h) \cdot \boldsymbol{\tau}_E|_E.$$

That is, along any line segment, the flux in that direction is a diffusion flux with variable coefficients  $\kappa_E$ . Note that  $\psi_E$  is unique up to a constant, and  $J(u_h) \cdot \boldsymbol{\tau}_E|_E$  is invariant to the constant change.

The local Nédélec space of the lowest order is defined as

$$\mathcal{N}_0(T) := (\mathcal{P}_0(T))^2 + \mathbf{x}^\perp \mathcal{P}_0(T),$$

where  $\mathbf{x}^\perp$  is a 90° rotation of  $\mathbf{x}$  satisfying  $\mathbf{x} \cdot \mathbf{x}^\perp = 0$ . Its DoFs for any  $\mathbf{v} \in \mathcal{N}_0(T)$  are defined as

$$\text{dof}_E(\mathbf{v}) = \frac{1}{|E|} \int_E \mathbf{v} \cdot \boldsymbol{\tau}_E \, ds = (\mathbf{v} \cdot \boldsymbol{\tau}_E)|_E.$$

Its canonical basis functions  $\{\chi_{E_j}\}_{j=1}^3 \subset \mathcal{N}_0(T)$  are obtained from  $\text{dof}_{E_i}(\chi_{E_j}) = \delta_{ij}$  for  $1 \leq i, j \leq 3$ . If we apply  $\text{dof}_E$  to  $\kappa_E^{-1} J(u_h)|_T$ , then we have

$$\begin{aligned} \text{dof}_E(\kappa_E^{-1} J(u_h)) &= \text{dof}_E(\nabla(e^{\psi_E} u_h)) \\ &= \delta_E(e^{\psi_E} u_h) := (e^{\psi_E} u_h)(\mathbf{x}_j) - (e^{\psi_E} u_h)(\mathbf{x}_i), \end{aligned} \quad (2.3)$$

where  $\mathbf{x}_i$  and  $\mathbf{x}_j$  are the endpoints of  $E$ , that is,  $\boldsymbol{\tau}_E = \mathbf{x}_j - \mathbf{x}_i$ . In the terminology of differential forms, the flux  $J(u_h)$  is a 2-form, and  $\kappa_E^{-1} J(u_h)$  is a 1-form. The functional  $\text{dof}_E$  is applied to the 1-form.

Define  $\bar{\kappa}_E$  as the harmonic average of  $\kappa_E = \alpha e^{-\psi_E}$  on  $E$ , i.e.,

$$\bar{\kappa}_E = \left( \frac{1}{|E|} \int_E \kappa_E^{-1} \, ds \right)^{-1}. \quad (2.4)$$

We look for a flux approximation  $J_T(u_h) \in \mathcal{N}_0(T)$  written as

$$J_T(u_h) = \sum_{E \subset \partial T} \text{dof}_E(\kappa_E^{-1} J(u_h)) \bar{\kappa}_E \chi_E = \sum_{E \subset \partial T} \delta_E(e^{\psi_E} u_h) \bar{\kappa}_E \chi_E,$$

where  $\bar{\kappa}_E$  can be considered an edgewise Hodge star mapping a 1-form  $\chi_E$  to a 2-form. The flux approximation  $J_T(u_h)$  is also invariant to the constant shift of  $\psi_E$  to  $\psi_E + c_E$ .

Moreover, we can express  $\nabla v_h$  in  $\mathcal{N}_0(T)$  as

$$\nabla v_h = \sum_{E \subset \partial T} (\nabla v_h \cdot \boldsymbol{\tau}_E) \chi_E = \sum_{E \subset \partial T} \delta_E(v_h) \chi_E.$$

As a result, the following auxiliary bilinear form is used in the discretization

$$\begin{aligned} B_{\mathcal{N}}^T(u_h, v_h) &:= \int_T J_T(u_h) \cdot \nabla v_h \, d\mathbf{x} \\ &= \sum_{E_i, E_j \subset \partial T} \bar{\kappa}_{E_i} \delta_{E_i}(e^{\psi_{E_i}} u_h) \delta_{E_j}(v_h) \int_T \chi_{E_i} \cdot \chi_{E_j} \, d\mathbf{x}. \end{aligned} \quad (2.5)$$

The mass matrix  $(\int_T \chi_{E_i} \cdot \chi_{E_j} \, d\mathbf{x})$  for  $\mathcal{N}_0(T)$  is in general a full matrix. We shall apply a mass lumping technique to make it diagonal.

## 2.4 Edge-Averaged Finite Element Scheme

To derive the EAFE scheme [32, 53], we approximate the bilinear form (2.5) using mass lumping. We let  $\{\lambda_i(\mathbf{x})\}_{i=1}^3 \subset \mathcal{P}_1(T)$  be the barycentric coordinates to the vertices  $\{\mathbf{x}_i\}_{i=1}^3$  in  $T \in \mathcal{T}_h$  and define

$$\omega_E^T := \frac{1}{2} \cot \theta_E^T = - \int_T \nabla \lambda_i \cdot \nabla \lambda_j \, d\mathbf{x} \quad \text{when} \quad \boldsymbol{\tau}_E = \mathbf{x}_j - \mathbf{x}_i.$$

Then, the mass lumping for the local mass matrix in  $\mathcal{N}_0(T)$  [26] is

$$\int_T \mathbf{v} \cdot \mathbf{w} \, d\mathbf{x} \approx \sum_{E \subset \partial T} \omega_E^T (\mathbf{v} \cdot \boldsymbol{\tau}_E)|_E (\mathbf{w} \cdot \boldsymbol{\tau}_E)|_E, \quad \forall \mathbf{v}, \mathbf{w} \in \mathcal{N}_0(T). \quad (2.6)$$

That is, we use the diagonal matrix  $\text{diag}(\omega_{E_1}^T, \omega_{E_2}^T, \omega_{E_3}^T)$  to approximate the  $3 \times 3$  dense matrix  $(\int_T \boldsymbol{\chi}_{E_i} \cdot \boldsymbol{\chi}_{E_j} \, d\mathbf{x})$ . The mass lumping is exact when  $\mathbf{v}, \mathbf{w} \in \nabla \mathcal{P}_1(T) \subset \mathcal{N}_0(T)$ . Consequently, we have

$$\begin{aligned} B_{\mathcal{N}}^T(u_h, v_h) &= \int_T J_T(u_h) \cdot \nabla v_h \, d\mathbf{x} \\ &\approx \sum_{E \subset \partial T} \omega_E^T \bar{\kappa}_E \delta_E(e^{\psi_E} u_h) \delta_E(v_h) =: B_h^T(u_h, v_h). \end{aligned}$$

The EAFE discrete problem is to find  $u_h \in V_h$  such that

$$\sum_{T \in \mathcal{T}_h} B_h^T(u_h, v_h) = F(v_h), \quad \forall v_h \in V_h. \quad (2.7)$$

In the EAFE bilinear form, it is clear to see  $\bar{\kappa}_E > 0$  and  $\delta_E(e^{\psi_E} \lambda_i) \delta_E(\lambda_j) = -e^{\psi_E(\mathbf{x}_i)} < 0$ . Therefore, the off-diagonal entries in the stiffness matrix of the EAFE bilinear form in (2.7) are nonpositive if and only if

$$\omega_E^T + \omega_{E'}^{T'} = \frac{1}{2} \cot \theta_E^T + \frac{1}{2} \cot \theta_{E'}^{T'} \geq 0,$$

for any interior edge  $E = \partial T \cap \partial T'$ , which is also equivalent to the Delaunay condition of  $\mathcal{T}_h$  in two dimensions. Hence, the stiffness matrix corresponding to the EAFE bilinear form is an  $M$ -matrix if and only if the stiffness matrix for the Poisson equation (computed by  $-\omega_E^T$ ) is an  $M$ -matrix.

In implementation, the coefficients  $\alpha$  and  $\boldsymbol{\beta}$  are approximated as a constant  $\alpha_E$  and a constant vector  $\boldsymbol{\beta}_E$  on each edge  $E \subset \partial T$ , respectively. For example,  $\alpha_E = (\alpha(\mathbf{x}_i) + \alpha(\mathbf{x}_j))/2$  and  $\boldsymbol{\beta}_E = (\boldsymbol{\beta}(\mathbf{x}_i) + \boldsymbol{\beta}(\mathbf{x}_j))/2$ . The edgewise potential function is given as  $\psi_E(\mathbf{x}) = \alpha_E^{-1} \boldsymbol{\beta}_E \cdot \mathbf{x}$ . Thus, the DoFs are explicitly expressed as

$$\begin{aligned} \bar{\kappa}_E \delta_E(e^{\psi_E} u_h) &= \alpha_E \mathbb{B}(\alpha_E^{-1} \boldsymbol{\beta}_E \cdot (\mathbf{x}_i - \mathbf{x}_j)) u_h(\mathbf{x}_j) \\ &\quad - \alpha_E \mathbb{B}(\alpha_E^{-1} \boldsymbol{\beta}_E \cdot (\mathbf{x}_j - \mathbf{x}_i)) u_h(\mathbf{x}_i), \end{aligned} \quad (2.8)$$

where  $\mathbb{B}(z)$  is the Bernoulli function,

$$\mathbb{B}(z) = \begin{cases} \frac{z}{e^z - 1} & z \neq 0, \\ 1 & z = 0. \end{cases} \quad (2.9)$$

Since the Bernoulli function is not even, the resulting matrix  $\mathbf{B}$  associated with the EAFE bilinear form  $B_h^T(\cdot, \cdot)$  is non-symmetric; that is,  $\mathbf{B}_{ij} \neq \mathbf{B}_{ji}$  in general.

### 3 Virtual Element Methods

This section introduces the essential definitions and fundamental theories of the VEMs. Let  $\mathcal{K}_h$  denote a decomposition of  $\Omega$  into polygonal elements  $K$  with a mesh size  $h = \max_{K \in \mathcal{K}_h} h_K$ , where  $h_K$  is the diameter of  $K$ . In a polygonal element  $K$ ,  $\mathbf{x}_i$  for  $1 \leq i \leq N_V$  denote vertices and  $E_j$  for  $1 \leq j \leq N_E$  denote edges, where  $N_V$  is the number of vertices and  $N_E$  is the number of edges. For a simple polygon,  $N_V = N_E$ . We label the indices of the vertices or edges counterclockwise. We denote scaled tangent vectors on the edges by  $\boldsymbol{\tau}_j = \mathbf{x}_{j+1} - \mathbf{x}_j$  for  $1 \leq j \leq N_E - 1$ , and  $\boldsymbol{\tau}_{N_E} = \mathbf{x}_1 - \mathbf{x}_{N_V}$ .

#### 3.1 The Lowest Order Nodal and Edge Virtual Spaces

We first introduce the lowest order local nodal space in [43, 46]. Let the boundary space be

$$B_1(\partial K) := \{v_h \in C^0(\partial K) : v_h|_E \in \mathcal{P}_1(E), \forall E \subset \partial K\}.$$

Then, the local nodal space [43, 46] is defined as

$$\mathcal{V}_1(K) := \{v_h \in H^1(K) : v_h|_{\partial K} \in B_1(\partial K), \Delta v_h|_K = 0\},$$

and its DoFs are given as the values of  $v_h$  at the vertices of  $K$ , i.e.,

$$\text{dof}_i(v_h) = v_h(\mathbf{x}_i), \quad 1 \leq i \leq N_V. \quad (3.1)$$

The dimension of  $\mathcal{V}_1(K)$  is  $N_V$ , and its canonical basis,  $\{\phi_j\}_{j=1}^{N_V} \subset \mathcal{V}_1(K)$ , is defined by  $\text{dof}_i(\phi_j) = \delta_{ij}$ . It has been proved in [43] that the DoFs (3.1) are unisolvent for  $\mathcal{V}_1(K)$ . We also highlight that  $\mathcal{P}_1(K) \subseteq \mathcal{V}_1(K)$ , and the local  $H^1$ -projection is computable using the DoFs (3.1), that is,  $\Pi_1^\nabla : \mathcal{V}_1(K) \rightarrow \mathcal{P}_1(K)$  with

$$\begin{aligned} \int_K (\nabla \Pi_1^\nabla v_h - \nabla v_h) \cdot \nabla p_1 \, d\mathbf{x} &= 0, \quad \forall p_1 \in \mathcal{P}_1(K), \\ \int_{\partial K} (\Pi_1^\nabla v_h - v_h) \, ds &= 0. \end{aligned}$$

The global nodal space is defined as

$$\mathcal{V}_1(\mathcal{K}_h) := \{v_h \in H_0^1(\Omega) : v_h|_K \in \mathcal{V}_1(K), \forall K \in \mathcal{K}_h\},$$

and its global DoFs are all the values of  $v_h$  at the internal vertices of  $\mathcal{K}_h$ .

We introduce the lowest order edge space with reduced DoFs [47, 49],

$$\begin{aligned} \mathcal{N}_0(K) = \{\mathbf{v}_h \in H(\text{div}; K) \cap H(\text{rot}; K) : \text{div } \mathbf{v}_h &= 0, \text{rot } \mathbf{v}_h \in \mathcal{P}_0(K), \\ \mathbf{v}_h \cdot \boldsymbol{\tau}_E &\in \mathcal{P}_0(E), \forall E \subset \partial K\}, \end{aligned}$$

where  $\text{rot } \mathbf{v} = \partial v_2 / \partial x - \partial v_1 / \partial y$  for a vector  $\mathbf{v} = \langle v_1, v_2 \rangle$ . The DoFs for  $\mathcal{N}_0(K)$  [44, 45, 47, 49] use the lowest order edge moments, similar to those of  $\mathcal{N}_0(T)$ ,

$$\text{dof}_E(\mathbf{v}_h) = \frac{1}{|E|} \int_E \mathbf{v}_h \cdot \boldsymbol{\tau}_E \, ds = (\mathbf{v}_h \cdot \boldsymbol{\tau}_E)|_E, \quad (3.2)$$

for each edge  $E \subset \partial K$ , and the canonical basis,  $\{\boldsymbol{\chi}_j\}_{j=1}^{N_E} \subset \mathcal{N}_0(K)$ , is defined by  $\text{dof}_{E_i}(\boldsymbol{\chi}_j) = \delta_{ij}$  for  $1 \leq i \leq N_E$ . Note that, unlike the finite element spaces, explicit forms of  $\{\boldsymbol{\chi}_j\}_{j=1}^{N_E} \subset \mathcal{N}_0(K)$  are unknown. Instead, only the DoFs are used to construct a discretization.

By integration by parts,  $\text{rot } \mathbf{v}_h$  is determined by the DoFs (3.2), so the dimension of  $\mathcal{N}_0(K)$  is  $N_E$ . It is easy to verify the unisolvence for  $\mathcal{N}_0(K)$  because the divergence-free condition implies  $\mathbf{v}_h = \text{rot } \vartheta = \langle \partial \vartheta / \partial y, -\partial \vartheta / \partial x \rangle$  for some differentiable function  $\vartheta$ , and integration by parts leads to

$$\begin{aligned} \int_K |\mathbf{v}_h|^2 \, d\mathbf{x} &= \int_K \mathbf{v}_h \cdot \text{rot } \vartheta \, d\mathbf{x} \\ &= \int_K (\text{rot } \mathbf{v}_h) \vartheta \, d\mathbf{x} - \sum_{E \subset \partial K} \frac{1}{|E|} \int_E (\mathbf{v}_h \cdot \boldsymbol{\tau}_E) \vartheta \, ds. \end{aligned}$$

We also emphasize that  $\mathcal{N}_0(K)$  reduces to the local Nédélec space  $\mathcal{N}_0(T)$  when  $K$  is a triangle, and the local  $L^2$ -projection  $\Pi_0^0 : \mathcal{N}_0(K) \rightarrow (\mathcal{P}_0(K))^2$  is computable by the DoFs (3.2),

$$\begin{aligned} \int_K \mathbf{v}_h \cdot \mathbf{p}_0 \, d\mathbf{x} &= \int_K \mathbf{v}_h \cdot \text{rot } p_1 \, d\mathbf{x} \\ &= \int_K (\text{rot } \mathbf{v}_h) p_1 \, d\mathbf{x} - \sum_{E \subset \partial K} \frac{1}{|E|} \int_E (\mathbf{v}_h \cdot \boldsymbol{\tau}_E) p_1 \, ds, \end{aligned}$$

for some  $p_1 \in \mathcal{P}_1(K)$  with  $\text{rot } p_1 = \mathbf{p}_0$ .

The global edge virtual element space is constructed to preserve the  $H(\text{curl})$  conformity [44, 45, 49] with respect to the space

$$H_0(\text{rot}; \Omega) = \{\mathbf{v} \in (L^2(\Omega))^2 : \text{rot } \mathbf{v} \in L^2(\Omega), \mathbf{v} \cdot \mathbf{t} = 0 \text{ on } \partial\Omega\},$$

where  $\mathbf{t}$  denotes the unit tangent vector. Hence, the two-dimensional global space is defined as

$$\mathcal{N}_0(\mathcal{K}_h) := \{\mathbf{v}_h \in H_0(\text{rot}; \Omega) : \mathbf{v}_h|_K \in \mathcal{N}_0(K), \forall K \in \mathcal{K}_h\},$$

The global DoFs are  $\mathbf{v}_h \cdot \boldsymbol{\tau}_E$  for all interior edges of the decomposition  $\mathcal{K}_h$ .

We present an important relation between the local nodal space  $\mathcal{V}_1(K)$  and the local edge space  $\mathcal{N}_0(K)$ . The detailed proof can be found in [45].

**Proposition 1**  $\nabla \mathcal{V}_1(K)$  is a subspace of  $\mathcal{N}_0(K)$ , and moreover

$$\nabla \mathcal{V}_1(K) = \{\mathbf{v}_h \in \mathcal{N}_0(K) \mid \text{rot } \mathbf{v}_h = 0\}.$$

In addition, we show the relation between the canonical basis functions  $\{\phi_i\}_{i=1}^{N_V}$  for  $\mathcal{V}_1(K)$  and  $\{\chi_j\}_{j=1}^{N_E}$  for  $\mathcal{N}_0(K)$ .

**Lemma 1** For the canonical basis  $\chi_m, \chi_n \in \mathcal{N}_0(K)$  with  $1 \leq m < n \leq N_E$ , we have

$$\chi_n - \chi_m = - \sum_{l=m+1}^n \nabla \phi_l,$$

where  $\phi_l$  is the canonical basis of  $\mathcal{V}_1(K)$ .

**Proof** Let  $\mathbf{w}_h = - \sum_{l=m+1}^n \nabla \phi_l$ . Then,  $\mathbf{w}_h \in \nabla \mathcal{V}_1(K) \subset \mathcal{N}_0(K)$  by Proposition 1. It is clear to see that

$$\text{dof}_{E_i}(\mathbf{w}_h) = \text{dof}_{E_i}(\chi_n - \chi_m) = \begin{cases} 1 & \text{if } i = n, \\ -1 & \text{if } i = m, \\ 0 & \text{otherwise,} \end{cases}$$

for  $1 \leq i \leq N_E$ . Therefore,  $\mathbf{w}_h = \chi_n - \chi_m$  of  $\mathcal{N}_0(K)$  by the unisolvence condition.  $\square$



### 3.2 Bilinear Forms for the Poisson Equation

We introduce bilinear forms appearing in virtual element methods for the Poisson equation. The local continuous bilinear form for the Poisson equation is denoted as

$$a^K(u, v) = \int_K \nabla u \cdot \nabla v \, dx. \quad (3.3)$$

Since we do not know the explicit forms of  $u_h, v_h \in \mathcal{V}_1(K)$  inside  $K$ , it would not be possible to compute  $a^K(u_h, v_h)$  exactly. Therefore, we use the equivalent bilinear form [43, 46],

$$a_h^K(u_h, v_h) = \int_K \nabla \Pi_1^\nabla u_h \cdot \nabla \Pi_1^\nabla v_h \, dx + S^K(u_h - \Pi_1^\nabla u_h, v_h - \Pi_1^\nabla v_h) \quad (3.4)$$

for all  $u_h, v_h \in \mathcal{V}_1(K)$ . In this case, the stabilization term  $S^K$  needs to satisfy that there are positive constants  $c_0$  and  $c_1$  independent of  $h_K$  such that

$$c_0 a^K(v_h, v_h) \leq S^K(v_h, v_h) \leq c_1 a^K(v_h, v_h),$$

for every  $v_h \in \mathcal{V}_1(K)$  with  $\Pi_1^\nabla v_h = 0$ . These inequalities directly imply the norm equivalence,

$$\gamma_* a^K(v_h, v_h) \leq a_h^K(v_h, v_h) \leq \gamma^* a^K(v_h, v_h), \quad \forall v_h \in \mathcal{V}_1(K), \quad (3.5)$$

for some positive constants  $\gamma_*$  and  $\gamma^*$  independent of  $h_K$  (see [17, 43, 46] for details). Here, we introduce a general choice for  $S^K$ ,

$$S_V^K(u_h, v_h) := \sum_{i=1}^{N_V} \text{dof}_i(u_h) \text{dof}_i(v_h). \quad (3.6)$$

Another choice of the stabilization term is the  $H^{\frac{1}{2}}$ -inner product [14],

$$S_E^K(u_h, v_h) := \sum_{E \subset \partial K} \delta_E(u_h) \delta_E(v_h), \quad (3.7)$$

where  $\delta_E$  is defined in (2.3). The verification of norm equivalence (3.5) for (3.6) can be found in [17] and for (3.7) in [14], respectively.

In Section 4, we will present a discretization of VEMs based on the finite volume formulation requiring no stabilization.

### 3.3 Construction of the Right-Hand Side

We use the approximation technique [43] for the right-hand side. Let  $f_0^K$  be the best constant approximation of  $f$  on  $K$ . Then, we define

$$F_h(v_h) := \sum_{K \in \mathcal{K}_h} \int_K f_0^K \bar{v}_h \, dx = \sum_{K \in \mathcal{K}_h} |K| f_0^K \bar{v}_h, \quad \bar{v}_h := \frac{1}{N_V} \sum_{i=1}^{N_V} v_h(\mathbf{x}_i).$$

This approximation yields an optimal estimate [43],

$$F_h(v_h) - F(v_h) \leq Ch \left( \sum_{K \in \mathcal{T}_h} |f|_{H^1(K)}^2 \right)^{1/2} |v_h|_{H^1(\Omega)}. \quad (3.8)$$

## 4 A Finite Volume Bilinear Form With Virtual Element

In this section, we present a finite volume bilinear form for the Poisson equation corresponding to  $a^K(\cdot, \cdot)$  in (3.3) on Voronoi meshes with respect to dual Delaunay triangulations consisting of acute triangles. We employ piecewise constant approximations on dual edge patches inspired by [7] and show that the finite volume bilinear form is compatible with the virtual element space  $\mathcal{V}_1(\mathcal{K}_h)$  and stabilization-free.

### 4.1 Voronoi Meshes with Dual Delaunay Triangulations

In two dimensions, a Delaunay triangulation consists of triangles whose circumcircles contain no other vertices of the triangulation. This condition implies that the sum of the two angles opposite any internal edge is less than or equal to  $\pi$ . On the other hand, a Voronoi tessellation is a partitioning in which each seed point is associated with a region containing all points closer to it than to any other seed, measured by Euclidean distance. In a convex domain, the Delaunay and Voronoi tessellations are dual to each other: each vertex of the Delaunay triangulation corresponds to a Voronoi cell, and each circumcenter of a Delaunay triangle becomes a vertex of a Voronoi polygon. Furthermore, edges in one mesh are orthogonal to the corresponding edges in the dual mesh.

This dual configuration plays a central role in finite volume methods [23]. The use of two interrelated meshes is also closely related to staggered DG (SDG) methods [18, 30, 54] and mimetic finite difference (MFD) methods [38, 51]. The dual patches in our formulation correspond to dual meshes in SDG methods. The required orthogonality between primal and dual meshes introduces geometric constraints similar to those in finite volume and MFD methods (though some MFD methods [36] allow non-orthogonal meshes), making the mesh structure more specific than in SDG methods.

In this section, we assume all the triangles determined by interior nodes are acute; each triangle contains its circumcenter. Then, we generate a Voronoi mesh by connecting the neighboring circumcenters; each Voronoi cell contains a vertex of a Delaunay triangle. We consider the Voronoi mesh primary for cell-centered finite volume methods, while the Delaunay triangulation is dual (see the left figure in Figure 1). This primary mesh is considered a subclass of general Voronoi meshes whose dual Delaunay may include obtuse triangles.

On the boundary of the domain, we obtain Voronoi nodes by extending perpendicular bisectors of triangles' edges around the boundary, where additional corner Voronoi nodes may help to express the boundary more accurately. Boundary Delaunay nodes are located between two Voronoi nodes along the boundary, satisfying the orthogonality of the triangles' edges and the boundary. Hence, the control volumes (or triangles) in the dual Delaunay triangulation can cover the whole domain. However, since considering the zero boundary condition (1.1b), we exclude the control volumes containing the boundary Delaunay nodes and employ the one-to-one relationships between a control volume and a primary (Voronoi) vertex (see the right figure in Figure 1).

We let  $\mathcal{K}_h$  denote a primary Voronoi mesh with a dual Delaunay triangulation  $\mathcal{T}_h = \mathcal{K}_h^*$ , consisting of acute triangles with interior nodes. Each polygon  $K \in \mathcal{K}_h$  contains exactly one Delaunay vertex  $\mathbf{x}_K^*$  in its interior, and each interior Voronoi vertex corresponds to the circumcenter of a triangle  $T \in \mathcal{T}_h$ . Given an edge  $E$  of  $K$  and the vertex  $\mathbf{x}_K^*$ , a sub-triangle is formed within  $K$ . Each polygon  $K$  is thus subdivided into as many sub-triangles as it has edges, and every interior edge in  $\mathcal{K}_h$  is shared by two such sub-triangles. We let  $D_E$  denote the union of the two sub-triangles adjacent to edge  $E$ , and  $E^*$  the dual edge in  $\mathcal{T}_h$  contained

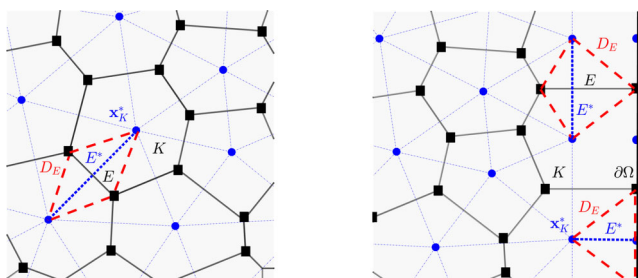


**Fig. 1** A primary Voronoi mesh with a dual Delaunay triangulation composed of acute triangles. Black squares indicate Voronoi nodes, while blue circles represent the seed points  $\mathbf{x}_K^*$  of the Voronoi polygons  $K$  (also referred to as Delaunay nodes). The edge  $E$  is shown as a solid black line, and its dual  $E^*$  appears as a blue dashed line. The dual edge patch  $D_E$  is enclosed by the red dashed lines. The left figure illustrates interior nodes, whereas the right figure highlights boundary nodes

within  $D_E$ , satisfying  $E^* \perp E$ . For a boundary edge  $E \subset \partial\Omega$ ,  $D_E$  consists of a single sub-triangle within  $\Omega$ , and  $E^*$  is defined as the shortest line segment from  $\mathbf{x}_K^*$  to edge  $E$ . The collection of all such dual edge patches  $D_E$  forms a polygonal mesh of the domain  $\Omega$ , denoted by  $\mathcal{D}_h$  (see Figure 1 for an illustration). If  $\mathbf{n}_{E^*}$  is a unit normal vector on  $E^*$  and  $\boldsymbol{\tau}_E$  is a scaled tangent vector on  $E$ , then  $\mathbf{n}_{E^*} = \boldsymbol{\tau}_E/|E|$  due to the orthogonality  $E^* \perp E$ . We also denote by  $\mathcal{E}_h^o$  the set of all interior edges in  $\mathcal{K}_h$ .

The assumption that  $\mathcal{T}_h$  consists of acute triangles guarantees that each dual patch  $D_E$  contains both the primal edge  $E$  and its orthogonal dual edge  $E^*$ . We denote the midpoint of  $E^*$  as  $\mathbf{m}_{E^*}$ , then by the property of the Voronoi mesh  $E^*$  and  $E$  intersect at  $\mathbf{m}_{E^*}$ , i.e.,  $\mathbf{m}_{E^*} = E^* \cap E$ . Thus,  $\mathbf{m}_{E^*}$  lies on  $E$  as well (though it is not necessarily the midpoint of  $E$ ). This geometric property is critical to the analysis of the proposed schemes for two key reasons: (1) evaluating a quantity, such as  $J_K(u_h)$ , at this point provides a consistent first-order approximation of the integral of this quantity over  $E^*$ ; and (2) it ensures the monotonicity of the proposed numerical schemes.

Finally, we recall the virtual element spaces on the primary Voronoi mesh and define function spaces on the dual triangulation and patches.

- $\mathcal{V}_1(\mathcal{K}_h) \subset H_0^1(\Omega)$ : the linear nodal virtual element space on the polygons  $K \in \mathcal{K}_h$ .
- $\mathcal{N}_0(\mathcal{K}_h) \subset H_0(\text{rot}; \Omega)$ : the lowest order edge virtual element space on the polygons  $K \in \mathcal{K}_h$ .
- $V_0(\mathcal{T}_h)$ : the set of piecewise constant functions  $v_h^*$  on the triangles  $T \in \mathcal{T}_h$ , excluding the control volumes containing the boundary Delaunay nodes.
- $W_0(\mathcal{D}_h)$ : the set of piecewise constant functions  $w_h$  on the edge patches  $D_E \in \mathcal{D}_h$ , where  $w_h|_{D_E} \equiv 0$  if  $E \subset \partial\Omega$ .

## 4.2 A Finite Volume Bilinear Form on Voronoi Meshes

We define a one-to-one map between  $\mathcal{V}_1(\mathcal{K}_h)$  and  $V_0(\mathcal{T}_h)$  by the DoFs. In each interior triangle  $T \in \mathcal{T}_h$ , there is only one interior Voronoi vertex  $\mathbf{x}_T$  because of the duality between  $\mathcal{K}_h$  and  $\mathcal{T}_h$ , so the DoFs of  $v_h \in \mathcal{V}_1(\mathcal{K}_h)$  at the vertex,  $v_h(\mathbf{x}_T)$ , maps to  $v_h^*|_T$  of  $v_h^* \in V_0(\mathcal{T}_h)$ . Through this one-to-one mapping, we can extend the definition of  $\delta_E$  to functions in  $V_0(\mathcal{T}_h)$ , i.e.,  $\delta_E(v_h^*) = \delta_E(v_h)$  is the difference of function values of  $v_h$  on the vertices of  $E$  following the orientation of  $E$ .

We consider a balance equation for the Poisson equation over each  $T \in \mathcal{T}_h$ ,

$$-\int_{\partial T} \nabla u \cdot \mathbf{n} \, ds = \int_T f \, d\mathbf{x}. \quad (4.1)$$

We define a normal flux approximation  $\mathcal{G}_{\mathbf{n}}(u_h) \in W_0(\mathcal{D}_h)$  as

$$\mathcal{G}_{\mathbf{n}}(u_h)|_{D_E} := \nabla u_h(\mathbf{m}_{E^*}) \cdot \mathbf{n}_{E^*} = \nabla u_h(\mathbf{m}_{E^*}) \cdot \frac{\boldsymbol{\tau}_E}{|E|} = \frac{\delta_E(u_h)}{|E|}. \quad (4.2)$$

A cell-centered finite volume method uses this piecewise constant  $\mathcal{G}_{\mathbf{n}}(u_h)$  as an approximation to the normal flux on  $E^* \subset D_E$

$$\int_{E^*} \nabla u_h \cdot \mathbf{n}_{E^*} \, ds \approx \int_{E^*} \mathcal{G}_{\mathbf{n}}(u_h) \, ds = \frac{|E^*|}{|E|} \delta_E(u_h).$$

For  $u_h$  in the virtual element space  $\mathcal{V}_1(\mathcal{K}_h)$ ,  $\nabla u_h \cdot \mathbf{n}_{E^*}$  is not computable but can be evaluated at the midpoint  $\mathbf{m}_{E^*}$ . By the duality, it equals to the tangential derivative along  $E$ , which is computable as  $u_h|_E$  is linear. Then, if  $\phi_T^* \in V_0(\mathcal{T}_h)$  is the characteristic function of a triangle  $T \in \mathcal{T}_h$ , i.e.  $\phi_T^* \equiv 1$  in  $T$  and  $\phi_T^* \equiv 0$  in  $\Omega \setminus T$ , the balance equation (4.1) implies a discrete problem

$$\sum_{E \in \mathcal{E}_h^o} \frac{|E^*|}{|E|} \delta_E(u_h) \delta_E(\phi_T^*) = \int_T f \, d\mathbf{x} = \int_{\Omega} f \phi_T^* \, d\mathbf{x} = F(\phi_T^*).$$

By using linear combinations in  $V_0(\mathcal{T}_h)$ , we define a local bilinear form

$$\mathbf{a}_h(u_h, v_h^*) := \sum_{E \in \mathcal{E}_h^o} \omega_E \delta_E(u_h) \delta_E(v_h^*), \quad \forall v_h^* \in V_0(\mathcal{T}_h),$$

where  $\omega_E := |E^*|/|E|$ . Therefore, the corresponding discrete problem is to find  $u_h \in \mathcal{V}_1(\mathcal{K}_h)$  such that

$$\mathbf{a}_h(u_h, v_h^*) = F(v_h^*), \quad \forall v_h^* \in V_0(\mathcal{T}_h), \quad (4.3)$$

which is a Petrov-Galerkin formulation of the Poisson equation. By changing  $\delta_E(v_h^*)$  to  $\delta_E(v_h)$ , we obtain a Galerkin formulation  $\mathbf{a}_h(u_h, v_h)$ .

In the virtual element framework, the bilinear form can be explained in terms of mass lumping in the edge virtual element space  $\mathcal{N}_0(K)$  for  $K \in \mathcal{K}_h$  (see also (2.6)),

$$\begin{aligned} a^K(u_h, v_h) &= \int_K \nabla u_h \cdot \nabla v_h \, d\mathbf{x} \approx \sum_{E \subset \partial K} \frac{1}{2} \omega_E (\nabla u_h \cdot \boldsymbol{\tau}_E)|_E (\nabla v_h \cdot \boldsymbol{\tau}_E)|_E \\ &= \sum_{E \subset \partial K} \frac{1}{2} \omega_E \delta_E(u_h) \delta_E(v_h^*) =: \mathbf{a}_h^K(u_h, v_h^*), \quad \forall v_h^* \in V_0(\mathcal{T}_h) \end{aligned} \quad (4.4)$$

because  $(\nabla v_h \cdot \boldsymbol{\tau}_E)|_E = \delta_E(v_h)$ . Moreover, we emphasize that the DoFs of  $v_h \in \mathcal{V}_1(\mathcal{K}_h)$  compute the bilinear form  $\mathbf{a}_h^K(\cdot, \cdot)$  without any stabilization term, so the discretization (4.3) can be viewed as a stabilization-free virtual element method.

For the right-hand side, we apply mass lumping with the vertices of a triangle  $T \in \mathcal{T}_h$  by using the constant approximation  $f_0^K$  on  $K$  introduced in Section 3.3. More precisely, when the three vertices of  $T_j \in \mathcal{T}_h$  are in polygons  $K_1$ ,  $K_2$ , and  $K_3$  in  $\mathcal{K}_h$ , the right-hand side is calculated by

$$F(\phi_{T_j}^*) = \int_{\Omega} f \phi_{T_j}^* \, d\mathbf{x} \approx \frac{|T_j|}{3} (f_0^{K_1} + f_0^{K_2} + f_0^{K_3}) =: \mathcal{F}_h(\phi_{T_j}^*). \quad (4.5)$$

Moreover, by comparing  $\mathcal{F}_h(\phi_{T_j}^*)$  with  $F_h(\phi_{T_j})$  defined in Section 3.3, we observe that  $\mathcal{F}_h(\phi_{T_j}^*) = F_h(\phi_{T_j})$  when the polygons  $K_1$ ,  $K_2$ , and  $K_3$  are regular. However, they may differ when at least one of the polygons is not regular.

### 4.3 M-Matrix Property

We stress that the stiffness matrix corresponding to  $\mathbf{a}_h(\cdot, \cdot)$  is an  $M$ -matrix through the following lemma.

**Lemma 2** *If  $\mathcal{K}_h$  is a primary Voronoi mesh with a dual Delaunay triangulation consisting of acute triangles, then the stiffness matrix corresponding to  $\mathbf{a}_h(\cdot, \cdot)$  is an  $M$ -matrix.*

**Proof** Let  $\phi_j$  be a global nodal virtual function in  $\mathcal{V}_1(\mathcal{K}_h)$  such that  $\phi_j(\mathbf{x}_i) = \delta_{ij}$  for any internal vertex  $\mathbf{x}_i$  in  $\mathcal{K}_h$ . We consider the stiffness matrix whose entries are

$$\mathbf{A}_{ij} = \mathbf{a}_h(\phi_j, \phi_i) = -\omega_E = -|E^*|/|E| < 0.$$

The partition of unity implies that

$$\sum_i \mathbf{A}_{ij} = \mathbf{a}_h(\phi_j, 1) = 0$$

if  $\mathbf{x}_j$  has no neighbor on the boundary. If  $\mathbf{x}_j$  has a neighbor on the boundary, then  $\sum_i \mathbf{A}_{ij} > 0$ . Hence, the matrix from the bilinear form  $\mathbf{a}_h(\cdot, \cdot)$  is an invertible  $M$ -matrix.  $\square$

### 4.4 Convergence Analysis for Poisson Equation

We use an alternative form with the normal flux approximation (4.2) on the edge patches  $D_E$  for convergence analysis,

$$\mathbf{a}_h(u_h, v_h) = \sum_{E \in \mathcal{E}_h^o} \frac{|E^*|}{|E|} \delta_E(u_h) \delta_E(v_h) = 2 \sum_{E \in \mathcal{E}_h^o} \int_{D_E} \mathcal{G}_\mathbf{n}(u_h) \mathcal{G}_\mathbf{n}(v_h) \, d\mathbf{x} \quad (4.6)$$

for  $u_h, v_h \in \mathcal{V}_1(\mathcal{K}_h)$  because  $|E^*||E| = 2|D_E|$ .

**Theorem 1** *Assume that  $\mathcal{K}_h$  is a primary Voronoi mesh with a dual Delaunay triangulation consisting of acute triangles. Let the solution  $u \in H^2(\Omega) \cap H_0^1(\Omega)$ . Then, we have for  $u_h \in \mathcal{V}_1(\mathcal{K}_h)$  and  $\mathcal{G}_\mathbf{n}(u_h)$  in (4.2),*

$$\left( \sum_{E \in \mathcal{E}_h^o} \|\nabla u \cdot \mathbf{n}_{E^*} - \mathcal{G}_\mathbf{n}(u_h)\|_{L^2(D_E)}^2 \right)^{1/2} \leq Ch \|u\|_{H^2(\Omega)}.$$

**Proof** We adopt the idea of the analysis in [7]. We define two different approximations of the exact normal flux  $\nabla u \cdot \mathbf{n}_{E^*}$ . The first one,  $\bar{\mathcal{G}}_\mathbf{n}(u) \in W_0(\mathcal{D}_h)$ , is the average of the flux on  $E^* \subset D_E$ ,

$$\bar{\mathcal{G}}_\mathbf{n}(u)|_{D_E} := \frac{1}{|E^*|} \int_{E^*} \nabla u \cdot \mathbf{n}_{E^*} \, d\mathbf{s}$$

for each  $D_E \in \mathcal{D}_h$ . Then, it follows from the balance equation (4.1), the definitions of  $\bar{\mathcal{G}}_\mathbf{n}(u)$  and  $\mathcal{G}_\mathbf{n}(v_h)$ , and the fact  $|E^*||E| = 2|D_E|$  that

$$2 \sum_{E \in \mathcal{E}_h^o} \int_{D_E} \bar{\mathcal{G}}_\mathbf{n}(u) \mathcal{G}_\mathbf{n}(v_h) \, d\mathbf{x} = \sum_{E \in \mathcal{E}_h^o} |E^*| (\bar{\mathcal{G}}_\mathbf{n}(u)|_{D_E}) \delta_E(v_h^*) = F(v_h^*).$$

Hence, if we compare this equation with the discrete problem (4.3) applying (4.6), then we have the orthogonality

$$\sum_{E \in \mathcal{E}_h^o} \int_{D_E} (\mathcal{G}_{\mathbf{n}}(u_h) - \bar{\mathcal{G}}_{\mathbf{n}}(u)) \mathcal{G}_{\mathbf{n}}(v_h) \, d\mathbf{x} = 0, \quad \forall v_h \in \mathcal{V}_1(\mathcal{K}_h). \quad (4.7)$$

The second approximation,  $u_I \in \mathcal{V}_1(\mathcal{K}_h)$ , is the nodal value interpolant of  $u$  onto the virtual element space. Then, by the orthogonality (4.7), we obtain

$$\begin{aligned} & \sum_{E \in \mathcal{E}_h^o} \|\mathcal{G}_{\mathbf{n}}(u_h) - \bar{\mathcal{G}}_{\mathbf{n}}(u)\|_{L^2(D_E)}^2 \\ &= \sum_{E \in \mathcal{E}_h^o} \int_{D_E} (\mathcal{G}_{\mathbf{n}}(u_h) - \bar{\mathcal{G}}_{\mathbf{n}}(u)) (\mathcal{G}_{\mathbf{n}}(u_I) - \bar{\mathcal{G}}_{\mathbf{n}}(u)) \, d\mathbf{x} \\ &\leq \sum_{E \in \mathcal{E}_h^o} \|\mathcal{G}_{\mathbf{n}}(u_h) - \bar{\mathcal{G}}_{\mathbf{n}}(u)\|_{L^2(D_E)} \|\mathcal{G}_{\mathbf{n}}(u_I) - \bar{\mathcal{G}}_{\mathbf{n}}(u)\|_{L^2(D_E)}. \end{aligned}$$

Moreover, the Cauchy-Schwarz inequality implies that

$$\sum_{E \in \mathcal{E}_h^o} \|\mathcal{G}_{\mathbf{n}}(u_h) - \bar{\mathcal{G}}_{\mathbf{n}}(u)\|_{L^2(D_E)}^2 \leq \sum_{E \in \mathcal{E}_h^o} \|\mathcal{G}_{\mathbf{n}}(u_I) - \bar{\mathcal{G}}_{\mathbf{n}}(u)\|_{L^2(D_E)}^2.$$

Using the triangle inequality, we have

$$\begin{aligned} & \|\mathcal{G}_{\mathbf{n}}(u_I) - \bar{\mathcal{G}}_{\mathbf{n}}(u)\|_{L^2(D_E)} \\ & \leq \|\nabla u \cdot \mathbf{n}_{E^*} - \mathcal{G}_{\mathbf{n}}(u_I)\|_{L^2(D_E)} + \|\nabla u \cdot \mathbf{n}_{E^*} - \bar{\mathcal{G}}_{\mathbf{n}}(u)\|_{L^2(D_E)}. \end{aligned}$$

Each term means the first order approximation because  $\mathcal{G}_{\mathbf{n}}(u_I)$  equals  $\nabla u \cdot \mathbf{n}_{E^*}$  at a point on  $E \subset D_E$ , and  $\bar{\mathcal{G}}_{\mathbf{n}}(u)$  equals  $\nabla u \cdot \mathbf{n}_{E^*}$  at a point on  $E^* \subset D_E$ .  $\square$

## 5 A Monotone Edge-Averaged Virtual Element Method

In this section, we present a monotone virtual element scheme based on the finite volume approach introduced in Section 4. The main challenge in deriving EAVE methods, both the monotone EAVE (Section 5) and the general EAVE (Section 6), lies in defining a suitable local flux approximation  $J_K(u_h)$  for the flux  $J(u_h) = \alpha \nabla u_h + \beta u_h$  on polygonal elements, and in constructing bilinear forms that approximate  $J_K(u_h) \cdot \nabla v_h$  using quantities that are computable in an edge-based manner.

Let  $\mathcal{K}_h$  be a primary Voronoi mesh with a dual Delaunay triangulation  $\mathcal{T}_h = \mathcal{K}_h^*$  consisting of acute triangles (see Figure 1). We consider the same one-to-one map between  $\mathcal{V}_1(\mathcal{K}_h)$  and  $V_0(\mathcal{T}_h)$ , and the constant space  $W_0(\mathcal{D}_h)$  on the edge patches  $D_E \in \mathcal{D}_h$  as in Section 4.

For  $J_K(u_h) \in \mathcal{N}_0(K)$ ,  $J_K(u_h) \cdot \mathbf{n}_{E^*} = (J_K(u_h) \cdot \boldsymbol{\tau}_E)/|E|$  on each interior edge  $E \in \mathcal{E}_h^o$ . We define a flux approximation  $\mathcal{J}_{\mathbf{n}}(u_h) \in W_0(\mathcal{D}_h)$  in light of (2.3),

$$\mathcal{J}_{\mathbf{n}}(u_h)|_{D_E} := J_K(u_h)(\mathbf{m}_{E^*}) \cdot \mathbf{n}_{E^*} = \frac{\bar{\kappa}_E \delta_E(e^{\psi_E} u_h)}{|E|}, \quad (5.1)$$

where  $\psi_E$  is the edgewise potential function introduced in (2.2). The normal flux  $J_K(u_h) \cdot \mathbf{n}_{E^*}$  is computable at the intersection point  $\mathbf{m}_{E^*}$ .

Recall that the flux  $J(u) = \alpha \nabla u + \beta u$ . In a balance equation corresponding to the convection-diffusion equation (1.1a) over each  $T \in \mathcal{T}_h$ ,

$$-\int_{\partial T} J(u) \cdot \mathbf{n} \, ds = \int_T f \, dx, \quad (5.2)$$

the discrete flux  $\mathcal{J}_n(u_h)$  approximates the flux  $J(u_h) \cdot \mathbf{n}_{E^*}$  on each  $E^* \subset D_E$ ,

$$\int_{E^*} J(u_h) \cdot \mathbf{n}_{E^*} \, ds \approx \int_{E^*} \mathcal{J}_n(u_h) \, ds = \frac{|E^*|}{|E|} \bar{\kappa}_E \delta_E(e^{\psi_E} u_h).$$

By introducing  $\phi_T^* \in V_0(\mathcal{T}_h)$  such that  $\phi_T^* \equiv 1$  in  $T$  and  $\phi_T^* \equiv 0$  in  $\Omega \setminus T$ , a cell-centered finite volume method for the balance equation (5.2) is represented as

$$\sum_{E \in \mathcal{E}_h^o} \frac{|E^*|}{|E|} \bar{\kappa}_E \delta_E(e^{\psi_E} u_h) \delta_E(\phi_T^*) = \int_T f \, dx = F(\phi_T^*). \quad (5.3)$$

Thus, using linear combinations of such  $\phi_T^*$  in  $V_0(\mathcal{T}_h)$ , we define a bilinear form on  $K \in \mathcal{K}_h$ ,

$$\mathcal{B}_h(u_h, v_h^*) := \sum_{E \in \mathcal{E}_h^o} \omega_E \bar{\kappa}_E \delta_E(e^{\psi_E} u_h) \delta_E(v_h^*).$$

The corresponding discrete problem is to seek  $u_h \in \mathcal{V}_1(\mathcal{K}_h)$  such that

$$\mathcal{B}_h(u_h, v_h^*) = F(v_h^*), \quad \forall v_h^* \in V_0(\mathcal{T}_h), \quad (5.4)$$

which is a Petrov-Galerkin discretization for the convection-diffusion equation (1.1a).

We can also apply mass lumping to derive a Galerkin formulation

$$\int_K J_K(u_h) \cdot \nabla v_h \, dx \approx \sum_{E \subset K} \frac{\omega_E}{2} (J_K(u_h) \cdot \boldsymbol{\tau}_E)|_E (\nabla v_h \cdot \boldsymbol{\tau}_E)|_E =: \mathcal{B}_h^K(u_h, v_h).$$

This approach can be considered as a cell-centered finite volume Scharfetter-Gummel method. One can find a vertex-centered finite volume Scharfetter-Gummel method [2] when the primary mesh is a Delaunay triangulation and the dual one is a Voronoi mesh. The vertex-centered method is identical to the EAFE method [32, 53]. Also, a stable mimetic finite difference (MFD) method [1] is considered as a vertex-centered method.

**Corollary 1** *We assume that a polygonal mesh  $\mathcal{K}_h$  is a Voronoi mesh with a dual Delaunay triangulation consisting of acute triangles. For  $\alpha \in C^0(\bar{\Omega})$  and  $\beta \in (C^0(\bar{\Omega}))^2$ , the EAVE method (5.4) is monotone, and consequently (5.4) is well-posed.*

**Proof** The proof is similar to that of Lemma 2, so we omit the proof.  $\square$

## 6 A General EAVE Method for Arbitrary Polygonal Meshes

This section presents the general EAVE method, an extension of the edge-averaged finite element (EAFE) stabilization to the virtual element framework on arbitrary polygonal meshes. In this formulation, we derive an EAVE bilinear form that remains compatible with the virtual element structure and supports general mesh geometries.

## 6.1 The General EAVE Method for Arbitrary Polygonal Meshes

We begin with the bilinear form with the flux approximation  $J_K(u_h) \in \mathcal{N}_0(K)$  in light of (2.3) and the definition of  $\bar{\kappa}_E$  in (2.4),

$$\int_K J_K(u_h) \cdot \nabla v_h \, d\mathbf{x} = \sum_{E \subset \partial K} \bar{\kappa}_E \delta_E(e^{\psi_E} u_h) \int_K \chi_E \cdot \nabla v_h \, d\mathbf{x}. \quad (6.1)$$

We then apply a mass lumping technique and Lemma 1 (see [33] for details). Let  $E_{ij}$  be the line segment joining  $\mathbf{x}_i$  and  $\mathbf{x}_j$  for  $i < j$  in  $K$ . Then, the EAVE bilinear form in a general polygon  $K$  is defined as

$$B_h^K(u_h, v_h) := \sum_{1 \leq i < j \leq N_V} \omega_{ij}^K \bar{\kappa}_{E_{ij}} \delta_{ij}^K(e^{\psi_{E_{ij}}} u_h) \delta_{ij}^K(v_h), \quad (6.2)$$

where  $\omega_{ij}^K = -a_h^K(\phi_i, \phi_j)$  in (3.4),  $\bar{\kappa}_{E_{ij}}$  is the harmonic average of  $\kappa_{E_{ij}}$ , and  $\delta_{ij}^K(v_h) = v_h(\mathbf{x}_j) - v_h(\mathbf{x}_i)$ . Thus, the corresponding discrete problem is to find  $u_h \in \mathcal{V}_1(\mathcal{K}_h)$  such that

$$\sum_{K \in \mathcal{K}_h} B_h^K(u_h, v_h) = F_h(v_h), \quad \forall v_h \in \mathcal{V}_1(\mathcal{K}_h). \quad (6.3)$$

**Remark 1** We note that  $\omega_{ij}^K = -a_h^K(\phi_i, \phi_j)$  in (6.2) is computable and already given in the virtual element methods for the Poisson equation. If we choose  $\omega_{ij}^K = -a_h^K(\phi_i, \phi_j)$  as in (4.3) on a Voronoi mesh corresponding to a Delaunay triangulation consisting of acute triangles, the general bilinear form (6.2) becomes the one in the monotone EAVE method (5.4). In practice, constant approximations  $\alpha_{E_{ij}}$  and  $\beta_{E_{ij}}$  on  $E_{ij}$  give a function  $\psi_{E_{ij}}(\mathbf{x}) = \alpha_{E_{ij}}^{-1} \beta_{E_{ij}} \cdot \mathbf{x}$  locally defined on  $E_{ij}$ . Therefore, the bilinear form is computed as

$$\begin{aligned} \bar{\kappa}_{E_{ij}} \delta_{E_{ij}}^K(e^{\psi_{E_{ij}}} u_h) &= \alpha_{E_{ij}} \mathbb{B}(\alpha_{E_{ij}}^{-1} \beta_{E_{ij}} \cdot (\mathbf{x}_i - \mathbf{x}_j)) u_h(\mathbf{x}_j) \\ &\quad - \alpha_{E_{ij}} \mathbb{B}(\alpha_{E_{ij}}^{-1} \beta_{E_{ij}} \cdot (\mathbf{x}_j - \mathbf{x}_i)) u_h(\mathbf{x}_i), \end{aligned}$$

where  $\mathbb{B}(\cdot)$  is the Bernoulli function defined in (2.9).

## 6.2 A Sufficient Condition for Monotonicity Property

The following lemma provides a sufficient condition under which the general EAVE method satisfies the monotonicity property.

**Lemma 3** *If the stiffness matrix for the Poisson equation with the virtual bilinear form (3.4) is an  $M$ -matrix, then the stiffness matrix from the EAVE method (6.3) is an  $M$ -matrix for  $\alpha \in C^0(\bar{\Omega})$  and  $\beta \in (C^0(\bar{\Omega}))^2$ .*

**Proof** It suffices to show that the off-diagonal components of the stiffness matrix are nonpositive. For  $i \neq j$ , it is clear to see that  $\mathbf{B}_{ij} = 0$  if  $\mathbf{x}_i$  and  $\mathbf{x}_j$  are not the vertices of a polygon. Otherwise, we let  $\mathcal{K}_{ij}$  be the set of the polygons having both  $\mathbf{x}_i$  and  $\mathbf{x}_j$  as vertices. Then, each component becomes

$$\mathbf{B}_{ij} = \sum_{K \in \mathcal{K}_{ij}} B_h^K(\zeta_j, \zeta_i).$$

For any polygon  $K \in \mathcal{K}_{ij}$ , we have

$$B_h^K(\zeta_j, \zeta_i) = -\omega_{ij}^K \bar{\kappa}_{E_{ij}} e^{\psi_{E_{ij}}(\mathbf{x}_j)} \quad \text{or} \quad -\omega_{ji}^K \bar{\kappa}_{E_{ji}} e^{\psi_{E_{ji}}(\mathbf{x}_j)}.$$



Note that  $B_h^K(\zeta_j, \zeta_i)$  depends on the local indices of  $i$  and  $j$  which are determined counterclockwise in  $K$ . Hence, since  $\omega_{ij}^K = -a_h^K(\zeta_i, \zeta_j) \geq 0$  and  $\bar{\kappa}_{E_{ij}} > 0$ , we get  $\mathbf{B}_{ij} \leq 0$ .  $\square$

## 7 Numerical Experiments

In this section, we present numerical experiments to demonstrate the effect of the monotonicity property and to verify the optimal order of convergence across different mesh types. We begin by defining a mesh-dependent norm in the virtual element space  $\mathcal{V}_1(\mathcal{K}_h)$ , based on the bilinear form given in (3.4). This norm, denoted by

$$\|v_h\|_A := \left( \sum_{K \in \mathcal{K}_h} a_h^K(v_h, v_h) \right)^{1/2}, \quad \forall v_h \in \mathcal{V}_1(\mathcal{K}_h), \quad (7.1)$$

is referred to as the  $A$ -norm and is known to be equivalent to the standard  $H^1$ -norm due to the stability property of the bilinear form in (3.5). To assess the presence of spurious oscillations in the numerical solutions, we also compute a mesh-dependent  $L^\infty$ -norm defined by

$$\|v_h\|_\infty := \max_i (\text{dof}_i(|v_h|)), \quad \forall v_h \in \mathcal{V}_1(\mathcal{K}_h).$$

All numerical experiments are performed using the authors' implementation based on the *iFEM* package [15]. We consider the following benchmark problem:

**Example 1** Let the computational domain be  $\Omega = (0, 1) \times (0, 1)$ . We consider the convection-dominated problem presented in [22]:

$$-\nabla \cdot (\epsilon \nabla u + \beta u) = f \quad \text{in } \Omega, \quad (7.2a)$$

$$u = g \quad \text{on } \partial\Omega, \quad (7.2b)$$

where  $\epsilon \ll 1$  is the diffusion coefficient,  $\beta = \langle 0, -1 \rangle$ , and  $f \equiv 0$ . The exact solution to the problem is given by

$$u(x, y) = x \left( \frac{1 - e^{(y-1)/\epsilon}}{1 - e^{-2/\epsilon}} \right), \quad (7.3)$$

which exhibits a sharp boundary layer near  $y = 1$  as  $\epsilon$  becomes smaller.

### 7.1 Monotonicity Test on Voronoi Meshes With Dual Delaunay

In this test, we compare the proposed edge-averaged virtual element (EAVE) methods (5.4) and (6.3) with the standard virtual element method (VEM) on Voronoi meshes whose dual Delaunay triangulations consist of acute triangles. The methods considered are as follows:

- VEM: The lowest-order VEM [48] for general second-order elliptic problems;
- M-EAVE: The *monotone* EAVE method (5.4);
- EAVE: The *general* EAVE method (6.3).

We consider both hexagonal and unstructured Voronoi meshes, each with a dual Delaunay triangulation composed of acute triangles. In Figure 2, the blue dots represent the vertices of the Delaunay triangulation. It is evident that each triangle formed by these blue dots contains an internal Voronoi vertex.

**Fig. 2** Voronoi meshes corresponding to dual Delaunay triangulations with  $h = 2^{-3}$

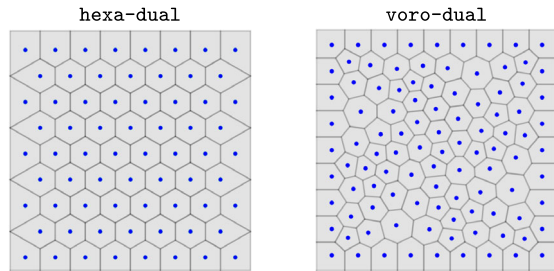


**Table 1** A mesh refinement study for VEM, M-EAVE, and EAVE with  $\epsilon = 10^{-2}$ .

hexa-dual						
$h$	VEM		M-EAVE		EAVE	
	$\ u_I - u_h\ _A$	Order	$\ u_I - u_h\ _A$	Order	$\ u_I - u_h\ _A$	Order
$2^{-3}$	2.097e+0	-	1.728e-1	-	1.631e-1	-
$2^{-4}$	1.792e+0	0.23	9.922e-2	0.80	1.058e-1	0.62
$2^{-5}$	6.154e-1	1.54	4.265e-2	1.22	5.062e-2	1.06
$2^{-6}$	2.096e-1	1.55	1.430e-2	1.58	1.737e-2	1.54
$h$	$\ u_I - u_h\ _\infty$	Order	$\ u_I - u_h\ _\infty$	Order	$\ u_I - u_h\ _\infty$	Order
$2^{-3}$	6.547e-1	-	4.358e-2	-	4.549e-2	-
$2^{-4}$	4.420e-1	0.57	1.912e-2	1.19	2.113e-2	1.11
$2^{-5}$	1.357e-1	1.70	5.871e-3	1.70	7.153e-3	1.56
$2^{-6}$	2.404e-2	2.50	1.295e-3	2.18	1.649e-3	2.12
voro-dual						
$h$	VEM		M-EAVE		EAVE	
	$\ u_I - u_h\ _A$	Order	$\ u_I - u_h\ _A$	Order	$\ u_I - u_h\ _A$	Order
$2^{-2}$	2.396e+0	-	2.425e-1	-	1.127e-1	-
$2^{-3}$	1.913e+0	0.33	1.682e-1	0.53	9.554e-2	0.24
$2^{-4}$	1.259e+0	0.60	1.005e-1	0.74	8.379e-2	0.19
$2^{-5}$	7.001e-1	0.85	4.647e-2	1.11	4.399e-2	0.93
$h$	$\ u_I - u_h\ _\infty$	Order	$\ u_I - u_h\ _\infty$	Order	$\ u_I - u_h\ _\infty$	Order
$2^{-2}$	6.978e-1	-	7.086e-2	-	3.291e-2	-
$2^{-3}$	4.705e-1	0.57	2.922e-2	1.28	1.829e-2	0.85
$2^{-4}$	3.237e-1	0.54	8.397e-3	1.80	9.731e-3	0.91
$2^{-5}$	1.637e-1	0.98	2.351e-3	1.84	3.972e-3	1.29

We solve the convection-dominated problem described in Example 1 and conduct a mesh refinement study using the VEM, M-EAVE, and EAVE methods on two types of Voronoi meshes with varying mesh sizes  $h$  and  $\epsilon = 10^{-2}$ . As shown in Table 1, all three methods—VEM, M-EAVE, and EAVE—show roughly first-order convergence in the  $A$ -norm as  $h \rightarrow 0$ , while the  $L^\infty$ -errors converge between first and second order. Compared to VEM, both M-EAVE and EAVE produce more stable and accurate solutions, especially on coarse meshes when  $h$  is not small enough compared to  $\epsilon$ . For smaller  $\epsilon$ , the regular VEM may show spurious oscillations;

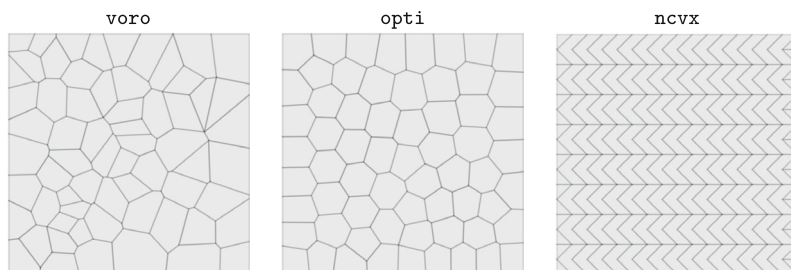


**Fig. 3** Various polygonal meshes with  $h = 2^{-3}$

**Table 2** A mesh refinement study for EAVE on various meshes with  $\epsilon = 10^{-2}$

$h$	voro		opti		ncvx	
	$\ u_I - u_h\ _A$	Order	$\ u_I - u_h\ _A$	Order	$\ u_I - u_h\ _A$	Order
$2^{-4}$	2.383e-1	-	1.078e-1	-	1.355e-1	-
$2^{-5}$	1.586e-1	0.59	6.250e-2	0.79	2.488e-2	2.45
$2^{-6}$	8.057e-2	0.98	2.914e-2	1.10	4.987e-3	2.32
$2^{-7}$	4.263e-2	0.92	1.414e-2	1.04	9.253e-4	2.43
$2^{-8}$	2.126e-2	1.00	6.902e-3	1.03	1.665e-4	2.47
$h$	$\ u_I - u_h\ _\infty$	Order	$\ u_I - u_h\ _\infty$	Order	$\ u_I - u_h\ _\infty$	Order
$2^{-4}$	3.714e-2	-	1.139e-2	-	2.563e-2	-
$2^{-5}$	1.494e-2	1.31	5.218e-3	1.13	3.551e-3	2.85
$2^{-6}$	4.183e-3	1.84	1.797e-3	1.54	5.052e-4	2.81
$2^{-7}$	1.224e-3	1.77	4.414e-4	2.03	6.625e-5	2.93
$2^{-8}$	3.123e-4	1.97	1.140e-4	1.95	8.424e-6	2.98

see Section 7.3, where the M-EAVE method, which satisfies the M-matrix condition, gives oscillation-free solutions. Although it is not easy to prove the monotonicity of the EAVE method, it still shows the behavior of a stabilized method for convection-dominated problems.

## 7.2 Accuracy Test on General Polygonal Meshes

This test verifies that the general EAVE method (6.3) is applicable to arbitrary polygonal meshes by evaluating its accuracy. To assess the method's performance, we conduct a mesh refinement study with varying mesh sizes  $h$  and fixed  $\epsilon = 10^{-2}$  across several polygonal mesh types. Specifically, we solve the problem described in Example 1 on the following mesh configurations (illustrated in Figure 3):

- **voro**: a Voronoi tessellation;
- **opti**: a Voronoi tessellation with cell shapes optimized using the Lloyd algorithm [42];
- **ncvx**: a structured mesh composed of non-convex polygons and triangles.

Table 2 shows the EAVE method's  $A$ -norm error and  $L^\infty$ -error for the **voro**, **opti**, and **ncvx** meshes.

Across all tested meshes, the  $A$ -norm errors exhibit at least first-order convergence, while the  $L^\infty$ -errors converge to zero at an approximate second-order rate. Notably, on the **ncvx**

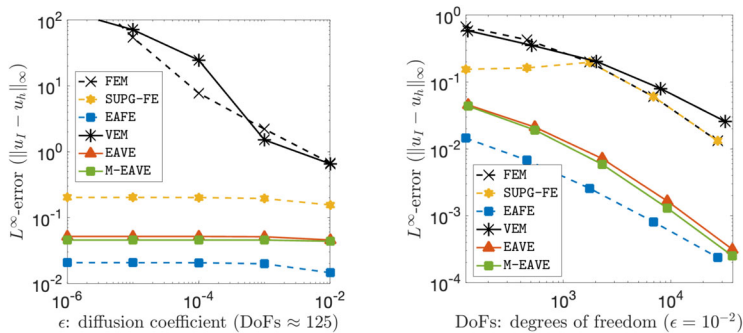


**Fig. 4** Error profiles of the numerical methods with varying  $\epsilon$  (left) and DoFs (right)

mesh, both the  $A$ -norm and  $L^\infty$ -errors demonstrate superconvergence. This behavior is attributed to the structured nature of the `ncvx` mesh and the alignment of its grid points with the boundary layer. These results confirm that the EAVE method delivers accurate and reliable numerical solutions on general polygonal meshes.

### 7.3 Test for Convection-Dominated Case

In this test, we evaluate the performance of the M-EAVE and EAVE methods in comparison with other standard and stabilized numerical methods for convection-dominated problems. All methods considered have the same expected order of convergence and are applied to solve the problem described in Example 1. The methods are listed as follows:

- FEM: Conforming finite element method with piecewise linear functions;
- SUPG-FE: Streamline-upwind Petrov-Galerkin method [10] with piecewise linear functions and the stabilization parameter

$$s_E = \frac{0.25h_T^2}{\epsilon P_e} \left(1 - \frac{1}{P_e}\right), \quad \text{where } P_e = \frac{\beta_T h_T}{2\epsilon},$$

with  $\beta_T = \|\beta\|_{L^\infty(T)}$  and  $h_T = |T|^{1/2}$ ;

- EAFE: Edge-averaged finite element method (2.7);
- VEM: The lowest-order VEM [48] for general second-order elliptic problems;
- M-EAVE: The *monotone* EAVE method (5.4);
- EAVE: The *general* EAVE method (6.3).

The performance of standard and stabilized numerical methods can be influenced by the presence of spurious oscillations in their solutions. According to the exact solution (7.3), numerical methods are expected to capture the boundary layer without introducing artificial oscillations. However, even if a method produces small  $H^1$ - or  $L^2$ -errors, local nonphysical oscillations may still arise—particularly when the discrete maximum principle (DMP) is not satisfied for the given mesh size. Such oscillations can be effectively detected using the  $L^\infty$ -error,  $\|u_I - u_h\|_\infty$ , where  $u_I$  denotes the nodal value interpolant of the exact solution  $u$ . To compare the robustness of the standard and stabilized methods, we solve the problem from Example 1 for various values of  $\epsilon$  and different numbers of degrees of freedom (DoFs), respectively.

Figure 4 presents the  $L^\infty$ -errors of the numerical methods under two testing scenarios: (i) varying the diffusion coefficient  $\epsilon$  from  $10^{-2}$  to  $10^{-6}$  while maintaining similar DoFs, and

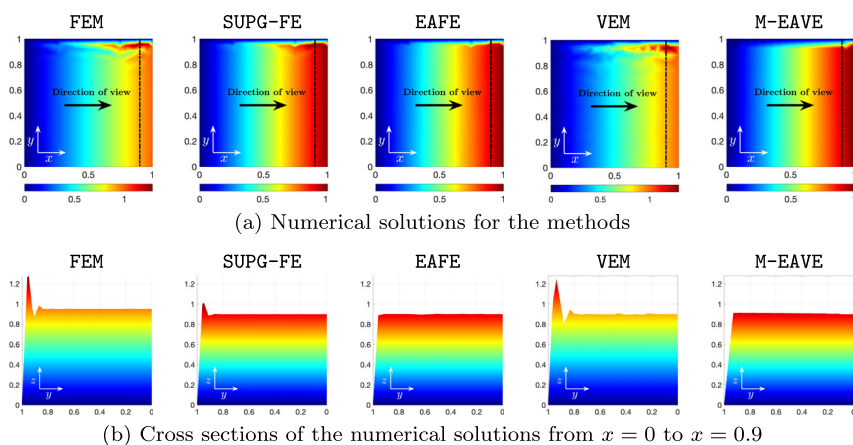


**Fig. 5** Comparison of the numerical solutions with  $\epsilon = 10^{-2}$  and  $h = 2^{-4}$ . **(a)** Numerical solutions for the methods **(b)** Cross sections of the numerical solutions from  $x = 0$  to  $x = 0.9$

(ii) varying mesh size from  $2^{-3}$  to  $2^{-7}$ , represented in terms of DoFs, with  $\epsilon = 10^{-2}$  fixed. As  $\epsilon$  decreases, the  $L^\infty$ -errors of the standard FEM and VEM increase rapidly, highlighting the necessity of stabilization techniques in convection-dominated regimes. In contrast, the  $L^\infty$ -errors of the stabilized methods—SUPG-FE, EAFE, M-EAVE, and EAVE—seem independent of  $\epsilon$ . With mesh refinement (i.e., increasing DoFs), all methods exhibit a decreasing trend in  $L^\infty$ -error with similar convergence rates. However, the edge-averaged methods (EAFE, M-EAVE, and EAVE) consistently produce errors nearly two orders of magnitude smaller than those of the SUPG-FE method.

To facilitate a quantitative comparison, Figure 5 displays the numerical solutions obtained using the FEM, SUPG-FE, EAFE, VEM, and M-EAVE methods with  $\epsilon = 10^{-2}$  and mesh size  $h = 2^{-4}$ , corresponding to a similar number of DoFs. Since the solution produced by the EAVE method is nearly identical to that of M-EAVE, it is omitted from the figure for brevity.

As expected, the numerical solutions obtained using the standard FEM and VEM exhibit spurious oscillations near the boundary layer, with the largest oscillation exceeding 20% of the maximum value of the exact solution. While the stabilized SUPG-FE method yields a more stable result compared to FEM, it still produces nonphysical oscillations with magnitudes over 10% of the exact solution. These oscillations can degrade the overall quality of the numerical solution and hinder the accurate resolution of sharp boundary layers. In contrast, the EAFE and M-EAVE methods satisfy the monotonicity property and produce oscillation-free solutions that effectively capture the sharp boundary layer. These results confirm that both the M-EAVE and EAVE methods provide high-quality approximations on polygonal meshes, particularly in convection-dominated regimes.

## 8 Conclusion

We have developed edge-averaged virtual element (EAVE) methods for convection dominated convection-diffusion problems by generalizing the edge-averaged finite element (EAFE) stabilization [53] to the virtual element setting. By incorporating a suitable flux approximation and mass lumping, we obtained a monotone EAVE method on Voronoi meshes whose dual

Delaunay triangulations consist of acute triangles. Using the Bernoulli function and the geometric structure of such meshes allows for efficient computation of the bilinear form, while the monotonicity ensures stable numerical solutions. In addition, we proposed a general EAVE method by deriving an alternative EAVE bilinear form applicable to arbitrary polygonal meshes. Our numerical experiments demonstrate the impact of monotonicity and confirm the optimal first-order convergence of the EAVE methods across various mesh types.

Extending the EAVE methods to three-dimensional problems is a natural direction for future research. Inspired by [3, 13, 16], we are also interested in exploring high-order Scharfetter-Gummel discretizations within the VEM framework, which pose additional challenges in preserving monotonicity. Moreover, the EAVE methods show strong potential for application-driven problems involving convection-dominated phenomena and complex geometries that require polygonal or polyhedral meshes.

**Acknowledgements** The authors would like to thank the anonymous reviewers for their valuable comments and suggestions.

**Funding** Long Chen's work was supported in part by the U.S. National Science Foundation grant NSF DMS-2309777 and DMS-2309785.

Shuhao Cao was supported in part by the U.S. National Science Foundation grant DMS-2309778.

**Data Availability** The datasets generated during and/or analyzed during the current study are available from the corresponding author upon reasonable request.

## Declarations

**Conflict of interest** The authors have not disclosed any competing interests.

## References

1. Adler, J.H., Cavanaugh, C., Hu, X., Huang, A., Trask, N.: A stable mimetic finite-difference method for convection-dominated diffusion equations. *SIAM Journal on Scientific Computing* **45**(6), A2973–A3000 (2023)
2. Bank, R.E., Coughran, W., Jr., Cowsar, L.C.: The finite volume Scharfetter-Gummel method for steady convection diffusion equations. *Computing and Visualization in Science* **1**(3), 123–136 (1998)
3. Bank, R.E., Vassilevski, P.S., Zikatanov, L.T.: Arbitrary dimension convection-diffusion schemes for space-time discretizations. *Journal of Computational and Applied Mathematics* **310**, 19–31 (2017)
4. Barrenechea, G.R., John, V., Knobloch, P., Rankin, R.: A unified analysis of algebraic flux correction schemes for convection-diffusion equations. *SeMA Journal* **75**(4), 655–685 (2018)
5. Benedetto, M.F., Berrone, S., Borio, A., Pieraccini, S., Scialó, S.: Order preserving SUPG stabilization for the virtual element formulation of advection-diffusion problems. *Computer Methods in Applied Mechanics and Engineering* **311**, 18–40 (2016)
6. Berrone, S., Borio, A., Manzini, G.: SUPG stabilization for the nonconforming virtual element method for advection-diffusion-reaction equations. *Computer Methods in Applied Mechanics and Engineering* **340**, 500–529 (2018)
7. Brezzi, F., Fortin, M., Marini, L.: Error analysis of piecewise constant pressure approximations of Darcy's law. *Computer Methods in Applied Mechanics and Engineering* **195**(13–16), 1547–1559 (2006)
8. Brezzi, F., Marini, L.D., Pietra, P.: Numerical simulation of semiconductor devices. *Computer Methods in Applied Mechanics and Engineering* **75**(1–3), 493–514 (1989)
9. Brezzi, F., Marini, L.D., Pietra, P.: Two-dimensional exponential fitting and applications to drift-diffusion models. *SIAM Journal on Numerical Analysis* **26**(6), 1342–1355 (1989)
10. Brooks, A.N., Hughes, T.J.: Streamline upwind/Petrov-Galerkin formulations for convection dominated flows with particular emphasis on the incompressible Navier-Stokes equations. *Computer Methods in Applied Mechanics and Engineering* **32**(1–3), 199–259 (1982)
11. Burman, E., Ern, A.: Stabilized Galerkin approximation of convection-diffusion-reaction equations: discrete maximum principle and convergence. *Mathematics of Computation* **74**(252), 1637–1652 (2005)

12. Burman, E., Hansbo, P.: Edge stabilization for Galerkin approximations of convection-diffusion-reaction problems. *Computer Methods in Applied Mechanics and Engineering* **193**(15–16), 1437–1453 (2004)
13. Cai, Z., Douglas, J., Jr., Park, M.: Development and analysis of higher order finite volume methods over rectangles for elliptic equations. *Advances in Computational Mathematics* **19**, 3–33 (2003)
14. Cao, S., Chen, L.: Anisotropic error estimates of the linear virtual element method on polygonal meshes. *SIAM Journal on Numerical Analysis* **56**(5), 2913–2939 (2018)
15. Chen, L.: iFEM: An Integrated Finite Element Methods Package in MATLAB. Technical Report, University of California at Irvine (2009)
16. Chen, L.: A new class of high order finite volume methods for second order elliptic equations. *SIAM Journal on Numerical Analysis* **47**(6), 4021–4043 (2010). <https://doi.org/10.1137/080720164>
17. Chen, L., Huang, J.: Some error analysis on virtual element methods. *Calcolo* **55**(1), 1–23 (2018)
18. Chen, L., Huang, X., Park, E.J., Wang, R.: A primal staggered discontinuous Galerkin method on polytopal meshes. *arXiv preprint arXiv:2410.23865* (2024)
19. Ciarlet, P.G., Raviart, P.A.: Maximum principle and uniform convergence for the finite element method. *Computer Methods in Applied Mechanics and Engineering* **2**(1), 17–31 (1973)
20. Cockburn, B.: Discontinuous Galerkin methods for convection-dominated problems. In: *High-Order Methods for Computational Physics*, pp. 69–224. Springer (1999)
21. Dörfler, W.: Uniform error estimates for an exponentially fitted finite element method for singularly perturbed elliptic equations. *SIAM Journal on Numerical Analysis* **36**(6), 1709–1738 (1999)
22. Elman, H.C., Silvester, D.J., Wathen, A.J.: *Finite Elements and Fast Iterative Solvers: with Applications in Incompressible Fluid Dynamics*. Numerical Mathematics and Science (2014)
23. Eymard, R., Gallouët, T., Herbin, R.: Finite volume methods. *Handbook of Numerical Analysis* **7**, 713–1018 (2000)
24. Gilbarg, D., Trudinger, N.S.: *Elliptic Partial Differential Equations of Second Order*, vol. 224. Springer (1977)
25. Godunov, S.K.: A difference method for numerical calculation of discontinuous solutions of the equations of hydrodynamics. *Matematicheskii Sbornik* **47**(89), 271–306 (1959)
26. Haugazeau, Y., Lacoste, P.: Condensation de la matrice de masse pour les éléments finis mixtes de  $h$  (rot). *Comptes rendus de l'Académie des sciences. Série I, Mathématique* **316**(5), 509–512 (1993)
27. John, V., Knobloch, P.: On spurious oscillations at layers diminishing (SOLD) methods for convection-diffusion equations: Part I-A review. *Computer Methods in Applied Mechanics and Engineering* **196**(17–20), 2197–2215 (2007)
28. Johnson, C., Saranen, J.: Streamline diffusion methods for the incompressible euler and navier-stokes equations. *Mathematics of Computation* **47**(175), 1–18 (1986)
29. Kikuchi, F.: Discrete maximum principle and artificial viscosity in finite element approximations to convective diffusion equations. Tokyo, University, Institute of Space and Aeronautical Science, Report no. 550 **42**, 153–166 (1977)
30. Kim, H.H., Chung, E.T., Lee, C.S.: A staggered discontinuous Galerkin method for the Stokes system. *SIAM Journal on Numerical Analysis* **51**(6), 3327–3350 (2013)
31. Knobloch, P.: A generalization of the local projection stabilization for convection-diffusion-reaction equations. *SIAM Journal on Numerical Analysis* **48**(2), 659–680 (2010)
32. Lazarov, R.D., Zikatanov, L.T.: An exponential fitting scheme for general convection-diffusion equations on tetrahedral meshes. *arXiv:1211.0869* (2012)
33. Lee, S.: Edge-averaged virtual element methods for convection-diffusion problems. University of California, Irvine (2021)
34. Li, Y., Feng, M.: A local projection stabilization virtual element method for convection-diffusion-reaction equation. *Applied Mathematics and Computation* **411**, 126536 (2021)
35. Li, Y., Zikatanov, L.T.: New stabilized  $P_1 \times P_0$  finite element methods for nearly inviscid and incompressible flows. *Computer Methods in Applied Mechanics and Engineering* **393**, 114815 (2022)
36. Lipnikov, K., Morel, J., Shashkov, M.: Mimetic finite difference methods for diffusion equations on non-orthogonal non-conformal meshes. *Journal of Computational Physics* **199**(2), 589–597 (2004)
37. Markowich, P.A., Zlámal, M.A.: Inverse-average-type finite element discretizations of selfadjoint second-order elliptic problems. *Mathematics of Computation* **51**(184), 431–449 (1988)
38. Rodrigo, C., Gaspar, F.J., Hu, X., Zikatanov, L.: A finite element framework for some mimetic finite difference discretizations. *Computers & Mathematics with Applications* **70**(11), 2661–2673 (2015)
39. Roos, H.G.: *Robust Numerical Methods for Singularly Perturbed Differential Equations*. Springer (2008)
40. Scharfetter, D.L., Gummel, H.K.: Large-signal analysis of a silicon read diode oscillator. *IEEE Transactions on Electron Devices* **16**(1), 64–77 (1969)
41. Stynes, M.: Steady-state convection-diffusion problems. *Acta Numerica* **14**, 445–508 (2005)



42. Talischi, C., Paulino, G.H., Pereira, A., Menezes, I.F.: PolyMesher: A general-purpose mesh generator for polygonal elements written in MATLAB. *Structural and Multidisciplinary Optimization* **45**(3), 309–328 (2012)
43. Beirão da Veiga, L., Brezzi, F., Cangiani, A., Manzini, G., Marini, L.D., Russo, A.: Basic principles of virtual element methods. *Mathematical Models and Methods in Applied Sciences* **23**(01), 199–214 (2013)
44. Beirão da Veiga, L., Brezzi, F., Dassi, F., Marini, L.D., Russo, A.: Virtual element approximation of 2D magnetostatic problems. *Computer Methods in Applied Mechanics and Engineering* **327**, 173–195 (2017)
45. Beirão da Veiga, L., Brezzi, F., Dassi, F., Marini, L.D., Russo, A.: Lowest order virtual element approximation of magnetostatic problems. *Computer Methods in Applied Mechanics and Engineering* **332**, 343–362 (2018)
46. Beirão da Veiga, L., Brezzi, F., Marini, L.D., Russo, A.: The hitchhiker’s guide to the virtual element method. *Mathematical Models and Methods in Applied Sciences* **24**(08), 1541–1573 (2014)
47. Beirão da Veiga, L., Brezzi, F., Marini, L.D., Russo, A.:  $H(\text{div})$  and  $H(\text{curl})$ -conforming virtual element methods. *Numerische Mathematik* **133**(2), 303–332 (2016)
48. Beirão da Veiga, L., Brezzi, F., Marini, L.D., Russo, A.: Virtual element method for general second-order elliptic problems on polygonal meshes. *Mathematical Models and Methods in Applied Sciences* **26**(04), 729–750 (2016)
49. Beirão da Veiga, L., Brezzi, F., Marini, L.D., Russo, A.: Serendipity face and edge VEM spaces. *Rendiconti Lincei* **28**(1), 143–180 (2017)
50. Beirão da Veiga, L., Dassi, F., Lovadina, C., Vacca, G.: SUPG-stabilized virtual elements for diffusion-convection problems: a robustness analysis. *ESAIM: Mathematical Modelling and Numerical Analysis* **55**(5), 2233–2258 (2021)
51. Beirão da Veiga, L., Lipnikov, K., Manzini, G.: The Mimetic Finite Difference Method for Elliptic Problems, vol. 11. Springer (2014)
52. Wu, S., Xu, J.: Simplex-averaged finite element methods for  $H(\text{grad})$ ,  $H(\text{curl})$ , and  $H(\text{div})$  convection-diffusion problems. *SIAM Journal on Numerical Analysis* **58**(1), 884–906 (2020)
53. Xu, J., Zikatanov, L.T.: A monotone finite element scheme for convection-diffusion equations. *Mathematics of Computation* **68**(228), 1429–1446 (1999)
54. Zhao, L., Park, E.J.: A new hybrid staggered discontinuous Galerkin method on general meshes. *Journal of Scientific Computing* **82**(1), 12 (2020)

**Publisher’s Note** Springer Nature remains neutral with regard to jurisdictional claims in published maps and institutional affiliations.

Springer Nature or its licensor (e.g. a society or other partner) holds exclusive rights to this article under a publishing agreement with the author(s) or other rightsholder(s); author self-archiving of the accepted manuscript version of this article is solely governed by the terms of such publishing agreement and applicable law.